

## THE *CHANDRA* DEEP FIELD NORTH SURVEY. XII. THE LINK BETWEEN FAINT X-RAY AND RADIO SOURCE POPULATIONS

F. E. BAUER,<sup>1</sup> D. M. ALEXANDER,<sup>1</sup> W. N. BRANDT,<sup>1</sup> A. E. HORNSCHMEIER,<sup>1</sup> C. VIGNALI,<sup>1</sup>  
 G. P. GARMIRE,<sup>1</sup> AND D. P. SCHNEIDER<sup>1</sup>  
 Received 2002 May 13; accepted 2002 July 19

### ABSTRACT

We investigate the relationship between faint X-ray and 1.4 GHz radio source populations detected within 3' of the Hubble Deep Field North using the 1 Ms *Chandra* and 40  $\mu$ Jy VLA surveys. Within this region, we find that  $\approx 42\%$  of the 62 X-ray sources have radio counterparts and  $\approx 71\%$  of the 28 radio sources have X-ray counterparts; thus a 40  $\mu$ Jy VLA survey at 1.4 GHz appears to be well-matched to a 1 Ms *Chandra* observation. Among the different source populations sampled, we find that the majority of the 18 X-ray detected emission-line galaxies (ELGs) have radio and mid-infrared *ISOCAM* counterparts and appear to be luminous star-forming galaxies at  $z = 0.3$ – $1.3$ . Importantly, the radio-detected ELGs make up  $\approx 35\%$  of the X-ray source population at 0.5–8.0 keV X-ray fluxes between  $\approx (1\text{--}5) \times 10^{-16}$  erg cm<sup>−2</sup> s<sup>−1</sup> and signal the emergence of the luminous, high- $z$  starburst galaxy population in the X-ray band. We find that the locally-determined correlation between X-ray luminosities and 1.4 GHz radio luminosity densities of the late-type galaxies can easily be extended to include the luminous intermediate-redshift ELGs, suggesting that the X-ray and radio emission processes are generally associated in star-forming galaxies. This result implies that the X-ray emission can be used as an indicator of star formation rate for star-forming galaxies. Finally, we show that there appear to be two statistically distinct types of *ISOCAM*-detected star-forming galaxies: those with detectable radio and X-ray emission and those without. The latter type may have stronger mid-infrared emission-line features that increase their detectability at mid-infrared wavelengths.

*Subject headings:* galaxies: active — galaxies: starburst — X-rays: galaxies — Radio: galaxies

### 1. INTRODUCTION

At bright X-ray fluxes ( $\gtrsim 10^{-15}$  erg cm<sup>−2</sup> s<sup>−1</sup>), almost all extragalactic X-ray point sources are found to be active galactic nuclei (AGN; e.g., Bade et al. 1998; Schmidt et al. 1998; Akiyama et al. 2000; Bauer et al. 2000; Lehmann et al. 2001). At the faintest currently achievable levels, however, a large population of “normal” galaxies emerge (e.g., Brandt et al. 2001a, hereafter Paper IV; Hornschemeier et al. 2001, hereafter Paper II; Tozzi et al. 2001). These X-ray faint “normal” galaxies are often optically bright ( $I \lesssim 22$ ) and are predominantly identified as narrow emission-line galaxies with redshifts of  $z = 0.3$ – $1.3$ . The majority appear to have faint 15  $\mu$ m *ISOCAM* counterparts (Alexander et al. 2002, hereafter Paper XI), suggesting a close association with the strongly evolving luminous infrared (IR) starburst galaxy population (e.g., Elbaz et al. 2002). X-ray/IR correlations have also been found locally for late-type normal spiral and irregular galaxies (e.g., Fabbiano, Gioia, & Trinchieri 1988; David, Jones, & Forman 1992; Shapley, Fabbiano, & Eskridge 2001). Thus the study of optically bright, X-ray faint galaxies may provide important clues about the nature of star formation on cosmic timescales.

An equally good correspondence between X-ray faint galaxies and faint radio sources is perhaps to be expected, given (1) the X-ray/radio correlation found for local late-type normal spiral and irregular galaxies (e.g., Fabbiano et al. 1988; Shapley et al. 2001; Ranalli, Comastri, & Setti 2002), and (2) the tight relationship between radio and mid-IR/far-IR (MIR/FIR) emission found for star-forming galaxies both locally and at moderate redshifts (e.g., Helou, Soifer, & Rowan-Robinson 1985; Condon, Anderson, & Helou 1991; Price & Duric 1992; Shapley et al. 2001; Elbaz et al. 2002; Garrett 2002). Such a

correlation can be understood physically, since X-ray and radio emission are both tied to the evolution of massive stars in the form of mass-transfer in binaries and supernovae, respectively (e.g., Petre 1993; Bressan, Silva, & Granato 2002). Indeed, within the Hubble Deep Field North itself (HDF-N; Williams et al. 1996), the faint radio and X-ray populations share a large overlap ( $\sim 70\%$ ; Paper IV).

In this paper, we investigate in detail the observational properties of the faint X-ray/radio matched sources in the vicinity of the HDF-N using two of the deepest surveys ever performed at their respective wavelengths, the 1 Ms *Chandra* Deep Field North X-ray (CDF-N; Brandt et al. 2001b, hereafter Paper V) and the 40  $\mu$ Jy VLA 1.4 GHz radio (Richards 2000, hereafter R00) surveys. This work extends the results of Paper IV to a larger area and to deeper X-ray fluxes, and it examines in more detail the relationships between the X-ray, radio, and IR emission. To facilitate comparison with previous X-ray/IR matching results in Paper XI, we adhere to much of the procedure outlined in that study. We describe the selection of our X-ray and radio samples in §2, compare and contrast these samples in §3 and §4, and discuss implications in §5. Throughout this paper, we adopt  $H_0 = 65$  km s<sup>−1</sup> Mpc<sup>−1</sup>,  $\Omega_M = \frac{1}{3}$ , and  $\Omega_\Lambda = \frac{2}{3}$ . The Galactic column density toward the CDF-N is  $(1.6 \pm 0.4) \times 10^{20}$  cm<sup>−2</sup> (Stark et al. 1992). Coordinates are for the J2000 epoch.

### 2. SAMPLE CONSTRUCTION

To compare X-ray and radio sources in the CDF-N, we restricted our focus to a 3' radius region (28.3 arcmin<sup>2</sup>) centered on the HDF-N ( $\alpha_{2000} = 12^{\text{h}}36^{\text{m}}49^{\text{s}}.4$ ,  $\delta_{2000} = +62^\circ 12'58''$ ). This area was chosen because it has the deepest and most uniform coverage at both X-ray and radio wavelengths, and it contains

<sup>1</sup> Department of Astronomy & Astrophysics, 525 Davey Lab, The Pennsylvania State University, University Park, PA 16802.

a wealth of follow-up resources including hundreds of spectroscopic redshifts (e.g., Cohen et al. 2000; Dawson et al. 2001) and deep imaging in most astronomical wavelength bands (for a review see Ferguson, Dickinson, & Williams 2000). These ancillary data are extremely important for assessing the nature of the X-ray and radio source populations. Of particular relevance, much of the  $3'$  radius region overlaps with the *ISOCAM*  $15\mu\text{m}$  observations (Aussel et al. 1999).

### 2.1. X-ray-Detected Sample

The X-ray selected sample was chosen from sources detected in the 1 Ms CDF-N catalog of Paper V in one or more of the 0.5–2.0 keV (soft), 2–8 keV (hard), and 0.5–8.0 keV (full) bands using WAVDETECT (Freeman et al. 2002) with a false-positive probability threshold of  $1 \times 10^{-7}$  (for details see Paper V). Within  $3'$  of the HDF-N, there are 62 X-ray sources detected down to an on-axis point-source full-band flux limit of  $\approx 1 \times 10^{-16} \text{ erg cm}^{-2} \text{ s}^{-1}$ . Table 1 lists the properties of the sources in the X-ray-detected sample.

### 2.2. Radio-Detected Sample

The radio-selected sample was chosen from sources detected at 1.4 GHz in the VLA catalog of R00. Within  $3'$  of the HDF-N, there are 28 radio sources detected down to a  $5\sigma$  flux density limit of  $\approx 40 \mu\text{Jy}$ . This region also has deep VLA observations at 8.5 GHz (Richards et al. 1998, hereafter R98; R00). The 8.5 GHz observations probe down to a  $5\sigma$  flux density limit of  $\approx 9\text{--}20 \mu\text{Jy}$ , allowing spectral indices to be calculated for the majority of radio sources. We note that the sensitivity of the 1.4 GHz observations over the region of interest is very uniform, while that of the 8.5 GHz sharply falls off past a radius of  $\approx 2'$ . However, because the 1.4 GHz observations were performed using the VLA A-array, the completeness limit for extended radio sources larger than  $\sim 3.5''$  is somewhat higher ( $\lesssim 50 \mu\text{Jy}$ ; see section 3.1 of R00 for details). Thus, the R00 catalog may be incomplete for galaxies closer than  $z \sim 0.3$ . Table 2 gives the properties of the sources in the radio-detected sample.

### 2.3. Source Matching

Source matching was performed by cross-identifying X-ray and radio sources to *I*-band counterparts detected by Barger et al. (2002; for X-ray sources reported in Paper V) or Bauer et al. (2002; for radio sources which lack 1 Ms catalog counterparts). Radio and X-ray sources were matched to optical sources using a  $1''$  search radius, except in three cases where the extent of the optical galaxy was quite large: CXOHDFN J123637.0+621134 ( $\approx 10''$  optical diameter,  $1''.3$  X-ray/radio offset) and CXOHDFN J123641.8+621132 ( $\approx 5''$  optical diameter,  $1''.1$  X-ray/radio offset). To within positional errors, however, the X-ray and 1.4 GHz radio emission from the matched sources were spatially coincident in all cases.<sup>2</sup> Note that the  $1\sigma$  positional uncertainties between the three wavelength bands are  $\lesssim 0''.6$  within the  $3'$  radius region.

<sup>2</sup> In two galaxies, CXOHDFN J123641.8+621132 and CXOHDFN J123648.3+621426, the X-ray source is coincident with lower significance 1.4 GHz detections but not with higher significance 8.5 GHz detections (offsets are  $\approx 2''$  but still within the extents of the galaxies).

<sup>3</sup> This image is available at <http://www.cv.nrao.edu/~jkempner/vla-hdf/>.

<sup>4</sup> The radio spectral index is defined as  $S_\nu \propto \nu^{-\alpha}$ . Lower values of  $\alpha$  thus yield tighter constraints on the 1.4 GHz flux density.

<sup>5</sup> This source has an optical extent of  $\sim 6\text{--}10''$  and was perhaps “resolved out” by the VLA 1.4 GHz observations.

<sup>6</sup> All errors are taken from Tables 1 and 2 of Gehrels (1986) and correspond to the  $1\sigma$  level; these were calculated assuming Poisson statistics.

<sup>7</sup> A 44 MHz bandwidth was used to calculate the radio flux (R00), which in turn was used to calculate the flux ratio,  $f_X/f_{1.4 \text{ GHz}}$ .

There are 18 sources in common between the X-ray- and radio-detected samples. Given the relatively low surface density of X-ray and radio sources, however, we can search for lower significance radio and X-ray sources within the respective samples without introducing a significant number of spurious detections.

Lower significance radio counterparts to X-ray sources were determined in two ways. The first and most direct method was to measure  $3\text{--}5\sigma$  radio emission at the positions of unmatched X-ray sources using the AIPS task *jmf* on the publicly available 1.4 GHz radio image (R00).<sup>3</sup> Unfortunately, this image does not cover the entire  $3'$  region, and 18 sources from the X-ray-detected sample therefore have no measurable 1.4 GHz flux density limits. Nonetheless, five additional 1.4 GHz radio counterparts were found (see Table 2 for details). The probability of finding a  $> 3\sigma$  1.4 GHz radio source at the position of an unmatched X-ray source is  $< 0.02$ . The second method was to match X-ray sources to radio sources detected at 8.5 GHz (R98) but not at 1.4 GHz. Three additional radio sources were found in this manner, and 1.4 GHz flux density upper limits were assigned to these sources assuming a conservative spectral index of  $\alpha = 0.8$  (the typical value for a starburst galaxy; e.g., Yun, Reddy, & Condon 2001).<sup>4</sup> One of these sources, CXOHDFN J123637.0+621134, has a  $99 \mu\text{Jy}$  counterpart in the WSRT 1.4 GHz map of Garrett et al. (2000), and this WSRT value has been used in lieu of a VLA 1.4 GHz upper limit; see Table 1.<sup>5</sup> Including these additional sources, there are a total of  $26 (42^{+10}_{-8}\%)$  X-ray sources with radio counterparts.<sup>6</sup>

Lower significance X-ray counterparts to radio sources were determined using WAVDETECT on the soft-, hard-, and full-band 1 Ms CDF-N X-ray images with a false-positive probability threshold of  $1 \times 10^{-5}$ . Two additional low-significance X-ray matches to radio sources were found. The probability of finding an X-ray source at the position of a known radio source and with the above WAVDETECT threshold at random is  $< 0.003$ . Including these additional sources, there are a total of  $20 (71^{+20}_{-16}\%)$  radio sources with X-ray counterparts. This matching fraction is significantly higher than was reported with 221.9 ks (Paper II) but comparable to that found within the smaller HDF-N region with 479.7 ks (Paper IV).

## 3. BASIC PROPERTIES OF X-RAY/RADIO MATCHED OBJECTS

The overlap between the X-ray- and radio-detected samples is shown in Figure 1, with the dashed lines indicating constant ratios of X-ray-to-radio flux,  $f_X/f_{1.4 \text{ GHz}}$ .<sup>7</sup> We characterize the sources in terms of their full-band X-ray fluxes, rather than their soft- or hard-band fluxes as has traditionally been done in the past, because (1) the vast majority of the sources in the X-ray sample are detected in the full band (94% versus 81% in the soft band and 66% in the hard band) and (2) the full band more effectively separates obscured AGN from “normal” galaxies, especially when combined with optical magnitude information, since it incorporates both soft- and hard-band X-ray fluxes. For instance, a galaxy and a moderately-obscured AGN could potentially have comparable soft-band X-ray fluxes, but because

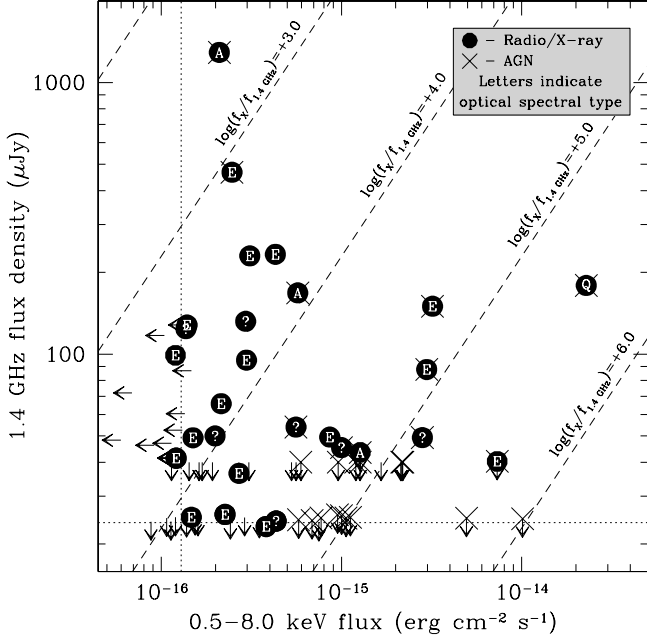


FIG. 1.— A comparison of 1.4 GHz flux density versus full-band X-ray flux for all X-ray and radio detected sources (i.e., detections at either 1.4 GHz or 8.5 GHz). Filled circles indicate X-ray/radio matched sources, while arrows signify source upper limits ( $3\sigma$  or  $5\sigma$  depending on if the source lies in within the publicly available 1.4 GHz image). Crosses indicate that AGN activity dominates either the X-ray or radio band (see §3). Letters represent spectroscopic identifications (e.g., Cohen et al. 2000; Dawson et al. 2001), with “E’s”, “A’s”, and “Q’s” denoting ELGs, ALGs, and broad-line AGN, respectively, while “?”s designate sources which remain unidentified (see Tables 1 and 2); for clarity, however, letters are plotted only for X-ray/radio matched sources. Lines of constant flux ratio are denoted by diagonal dashed lines, while the approximate detection limits of the X-ray and radio surveys are shown by vertical and horizontal dotted lines, respectively.

of their different spectral slopes (typically  $\Gamma \sim 2.0$  versus 1.0, respectively), the obscured AGN will have a much larger full-band flux and be easily identified.

We have adopted the source classification scheme presented in Paper XI with the exception that we further use the radio properties of the sources to identify AGN activity. This scheme is pivotal to all that follows and is thus repeated here. Since nearly all of the sources with  $l < 23$  have spectroscopic redshifts and classifications (e.g., Cohen et al. 2000; Dawson et al. 2001), sources were classified into three loose spectral types: emission-line galaxies (ELGs), and absorption-line galaxies (ALGs), and AGN-dominated sources. These categories are intended to identify qualitatively the bulk of the optical emission from a particular galaxy as either from active star formation, passively evolving stars, or AGN activity. Note, however, that in classifying the sources as ELGs and ALGs, we have ignored some of the subtleties of the optical spectral types — such as whether the emission-line spectra have H II-like emission lines indicative of active star formation or exhibit only a weak O II  $\lambda 3727$  doublet — since the spectra remain largely unpublished. Thus we caution that spectral misclassifications are possible for some sources.

We classified sources as ELGs if they have optical spectral classifications of “E”, “I”, “EI” or “EA” in Cohen et al. (2000). Likewise, we classified sources as ALGs if they have a classification of “A” in Cohen et al. (2000). AGN-dominated sources were identified based on one of the following criteria: a spectroscopic identification as a broad-line AGN (i.e., a “Q” spec-

tral type from Cohen et al. 2000), a rest-frame 0.5–8.0 keV luminosity  $> 3 \times 10^{42}$  erg s $^{-1}$ , an effective X-ray photon index  $\Gamma < 1.0$  (indicative of obscured AGN), or radio properties indicative of AGN (i.e., spectral indices  $\alpha < 0.4$ –0.5, radio jets/lobes, or variability; R98; Richards 1999, chap. 4, hereafter R99; R00). Any ELGs or ALGs that were determined to contain AGN were classed as AGN-dominated. Tables 1 and 2 list the spectral types of each source. In Figure 1, optical spectral types are represented by the letters “E” for ELGs, “A” for ALGs, “Q” for broad-line AGN, and “?” if the spectral type remains unknown, while AGN-dominated sources are indicated by large crosses.

Since the ratio of X-ray-to-radio flux found for classical AGN can span *several* orders of magnitude (e.g., Kellermann et al. 1989; Brinkmann et al. 2000; Bauer 2001, Fig. 4.10), it is not surprising to see such a large spread among the AGN in Figure 1 [ $\log(f_X/f_{1.4 \text{ GHz}}) \sim 3$ –6]. Less stringent AGN activity constraints can be placed on the fainter X-ray and radio sources because of their low signal-to-noise and some are therefore likely to host low-luminosity AGN. We note, however, that the large number of X-ray/radio matched ELGs at faint X-ray fluxes and radio flux densities is consistent with the emergence of a “normal,” star-forming galaxy population at moderate redshifts (e.g., Windhorst et al. 1985; R98; Paper II; Tozzi et al. 2001). Interestingly, there appears to be a steep rise in the number of radio matches to X-ray sources near the limit of the 1.4 GHz survey, suggesting that slightly deeper radio observations may detect several of the remaining X-ray sources.

The ubiquity of star formation within these X-ray/radio matched sources is most clearly demonstrated by comparing

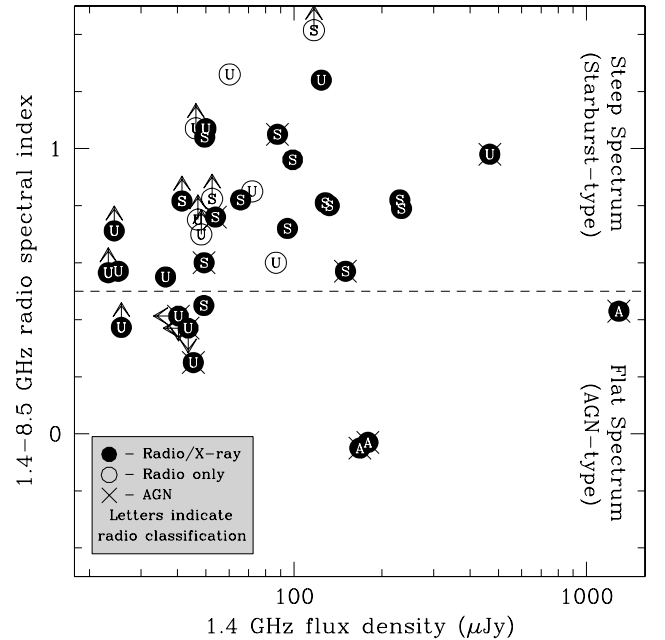


FIG. 2.— A comparison of 1.4–8.5 GHz spectral index ( $\alpha$ ) versus 1.4 GHz flux density for all radio sources. Filled circles indicate X-ray/radio matched sources, open circles denote unmatched radio sources, and arrows signify approximate  $3\sigma$  source upper or lower limits. Crosses indicate that AGN activity dominates either the X-ray or radio band (see §3). Letters represent the classifications of R99: “S’s” and “A’s” denote starbursts and AGNs, respectively, while sources with “U’s” remain unidentified. The horizontal dashed line denotes the typical spectral index,  $\alpha = 0.5$ , used to separate steep spectrum (starburst-type) and flat spectrum (AGN-type) systems (e.g., R00). The two X-ray/radio matches detected only at 8.5 GHz are shown as upper limits in both axes.

the 1.4–8.5 GHz radio spectral index to the 1.4 GHz flux density, as shown in Figure 2. Plotted are radio sources detected at either 1.4 or 8.5 GHz in the X-ray and radio samples, along with the AGN classifications outlined above (*crosses*) and the radio classifications from R99 (*letters*). These radio classifications — starburst-type sources (S), AGN candidates (A), and sources that could not be easily classified (referred to as unknown, or U) — are based primarily on radio spectral indices, morphologies, and angular sizes, but they also take into account optical and IR properties in some cases (see Muxlow et al. 1999 and R99). The radio classifications are intended to identify qualitatively the origin of the bulk of the radio emission from a particular galaxy and do not preclude the possibility of starburst-type sources having embedded AGN or AGN-type sources having stellar activity. When possible we have used the matched radio spectral indices provided in Table 1 of R99, where the 1.4 GHz and 8.5 GHz flux densities used to calculate the spectral indices were measured in their respective 3''5 convolved images. For the remaining sources — i.e., those with  $3\sigma$  detections at either 1.4 GHz or 8.5 GHz — we have estimated the spectral indices using the publicly available radio images; these lower significance estimates are noted in Tables 1 and 2 and should be treated as approximate since the images used to measure the fluxes were not matched in resolution. We also caution that variability among the radio AGN is a legitimate concern and could lead to inaccurate spectral index estimates since the two radio bands were observed two years apart. A horizontal dashed line denotes the typical spectral index,  $\alpha = 0.5$ , separating steep and flat spectrum radio sources. Steep spectral indices ( $\alpha \gtrsim 0.5$ ) often indicate radio emission from star formation, while flat ones ( $\alpha \lesssim 0.5$ ) often indicate emission from core-dominated AGN (e.g., Kellermann & Owen 1988). Within our sample area, there are 16 starburst-type, 3 AGN-type, and 17 unknown-type sources. As expected, nearly all of the X-ray-detected non-AGN sources are classified as starburst-type sources at radio wavelengths. Conversely, only approximately half of the X-ray/radio matched AGN are classified as AGN-type sources at radio wavelengths, suggesting that star formation activity is important in many of these AGN.

To explore further the nature of the X-ray and radio-selected samples, we compare the distribution of full-band X-ray flux to  $I$ -band magnitude (see Figure 3). Because of the empirical relationship between X-ray and optical emission in AGN (e.g., Elvis et al. 1994), this diagram highlights the degree and nature of any AGN activity. In the X-ray-optical plane, classical AGN typically have flux ratios of  $-1 \lesssim \log(f_X/f_I) \lesssim +1$ , while star-forming galaxies and low-luminosity AGN tend to have  $\log(f_X/f_I) \lesssim -1$  (e.g., Maccacaro et al. 1988; Stocke et al. 1991; Schmidt et al. 1998; Akiyama et al. 2000; Paper II; Shapley et al. 2001). These regions have been shaded and labeled for emphasis. We caution that although star formation generally appears to be the dominant emission mechanism for X-ray sources with  $\log(f_X/f_I) \lesssim -1$  (e.g., Paper II, Paper XI), X-ray emission from low-luminosity or heavily obscured AGN cannot be individually ruled out.

At first glance, the connection between X-ray and radio sources appears to be rather complex, as X-ray/radio matched counterparts (filled circles) span  $\sim 2$ – $3$  decades in both X-ray flux and optical magnitude. However, taking cues from the X-ray/IR matched sources of Paper XI, we notice a few interesting trends. First, the majority of the X-ray/radio matched sources that fall within the “galaxies” region of Figure 3

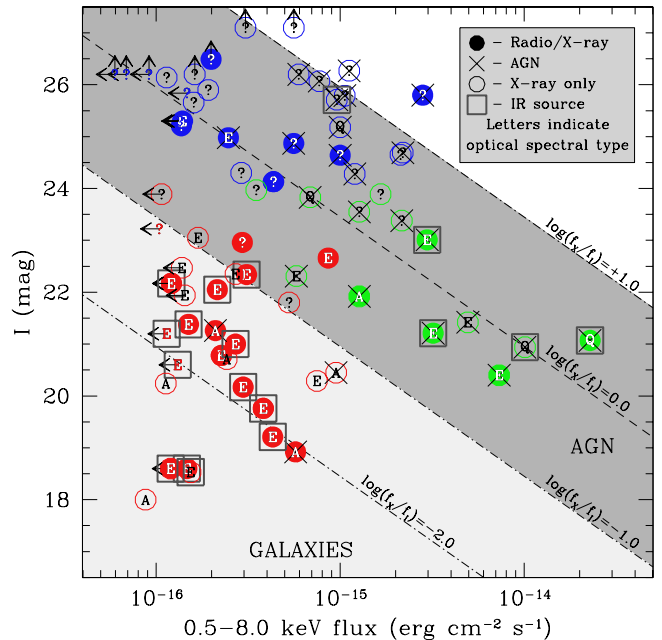


FIG. 3.— A comparison of  $I$ -band magnitude versus full-band X-ray flux for X-ray- and radio-detected sources. Filled circles indicate X-ray/radio matched sources, open circles denote unmatched X-ray sources, and arrows signify  $3\sigma$  source upper limits. The X-ray upper limits include both sources which remain undetected at X-ray energies and sources which are detected only in the soft or hard X-ray bands. As in Figure 1, crosses indicate that AGN activity dominates either the X-ray or radio band, and sources with letters represent spectroscopically identified sources (see §3). Additionally, large concentric squares indicate sources with *ISOCAM*  $15\mu\text{m}$  counterparts (Paper XI). Most of our  $3'$  radius region overlaps with the *ISOCAM*  $15\mu\text{m}$  observations; the 29 sources outside the *ISOCAM* region are noted in Tables 1 and 2. The colors of the sources indicate whether they were classified as galaxies (red), AGN (green), or optically faint sources (blue); see §3, as well as column 11 of Table 1 and column 13 of Table 2.

[i.e.,  $\log(f_X/f_I) \lesssim -1$ ] have IR counterparts (large concentric squares) and are spectroscopically identified as ELGs, compared to relatively few in the AGN region. As such, these sources appear to be distinct from the typical X-ray emitting AGN. The IR emission and ELG spectral types suggest that the X-ray emission in these sources is likely to be associated with active star-forming processes (Paper XI). Second, while there is no obvious division within the AGN population [i.e.,  $\log(f_X/f_I) \gtrsim -1$ ], an observational division occurs around  $I \approx 24$ . The optically bright X-ray/radio matches tend to be spectroscopically identified as galaxies or broad-line AGN with  $z \lesssim 1.0$ , while the optically fainter ones remain largely unclassified and perhaps comprise several different classes of object (see Alexander et al. 2001, hereafter Paper VI). Thus we divide the X-ray/radio matches into three basic categories: galaxies, optically bright ( $I < 24$ ) AGN, and optically faint ( $I \geq 24$ ) sources (see Figure 3, as well as column 12 of Table 1 and column 13 of Table 2). The three source types are highlighted in Figure 3 by the colors red, green, and blue, respectively.

#### 4. CATEGORIES OF X-RAY/RADIO MATCHED OBJECTS

Below we provide constraints on the basic nature of the sources in the “galaxies”, “optically bright AGN”, and “optically faint sources” categories.

#### 4.1. Galaxies

The “galaxies” sample includes 21 X-ray sources that lie within the  $\log(f_X/f_I) \lesssim -1$  region of Figure 3 and a further six sources that lie slightly above  $\log(f_X/f_I) = -1$ ; the latter sources are included since they share many characteristics with the former (these six sources are noted in Table 1). All but two of the 27 objects have X-ray luminosities below  $3 \times 10^{42}$  erg s<sup>-1</sup>. Fifteen of the 27 (56%) sources in the X-ray sample have radio counterparts, while 15 of the 18 (83%) sources in the radio sample have X-ray counterparts. Thus, it appears that the 40  $\mu$ Jy VLA survey at 1.4 GHz is extremely well-matched to the 1 Ms *Chandra* observation for the detection of galaxies.

In the nearby Universe, connections between X-ray, IR, and radio emission appear to split along evolutionary lines, with the strongest correlations arising from galaxies with active star formation, such as late-type spirals and irregulars (e.g., Shapley et al. 2001). A similar trend emerges in the CDF-N at moderate redshifts ( $z = 0.4\text{--}1.3$ ) for luminous IR starbursts and X-ray faint galaxies, as evidenced by the findings of Paper XI. X-ray faint galaxies with IR counterparts are predominantly identified spectroscopically as ELGs and exhibit no apparent X-ray/radio AGN activity, while those without IR counterparts are primarily ALGs and exhibit low-to-moderate level X-ray/radio AGN activity in roughly half of the cases. Since the ELGs and ALGs exhibit different properties, they are investigated separately below. We have assumed that the three “galaxies” sources which remain unclassified (i.e., sources with a “?”) are ALGs. These three objects were observed spectroscopically but the signal-to-noise of their spectra are too low to derive useful spectral types or redshifts. Given the optical magnitudes of the three sources, any strong emission lines would have been detected, implying that all three probably have absorption-line dominated continua.

##### 4.1.1. Emission-Line Galaxies

We find that 12 out of 18 (67%) X-ray-detected ELGs have radio counterparts, while 12 out of 14 (86%) radio-detected ELGs have X-ray counterparts. These matching fractions appear to corroborate the X-ray/IR trend found in Paper XI. Optically, all of the X-ray/radio matched ELGs reside within bright, extended galaxies and, when high-resolution, archival *HST* Flanking Field observations are available, have spiral, irregular, or merging morphologies. As shown in §3, the radio emission from the majority of the X-ray/radio matched ELG sources is indicative of star formation and yields an average radio spectral slope of  $\alpha = 0.76 \pm 0.04$ . In terms of their X-ray emission, however, the spectral constraints for individual sources are poor. We can, however, place good constraints on the nature of the X-ray emission from these ELGs in an average sense. When stacked together, the X-ray/radio detected ELGs have an average X-ray band ratio<sup>8</sup> of  $0.20 \pm 0.04$  (corresponding to  $\Gamma = 2.02 \pm 0.09$ ). This shows that the fraction of hidden AGN in these sources is low, similar to the findings of Paper XI for X-ray/IR ELGs, and that the radio and X-ray emission are more consistent with active star formation from normal galaxies (e.g., Condon 1992; Fabbiano 1989). Indeed, the luminosities of the X-ray/radio matched ELGs span the range expected from  $z \sim 0.1$  normal spiral systems up to powerful  $z \sim 1.3$  starbursts (i.e.,  $L_{1.4 \text{ GHz}} \sim 10^{20.7}\text{--}10^{24.3}$  W Hz<sup>-1</sup> and  $L_{0.5\text{--}8.0 \text{ keV}} \sim 10^{39.8}\text{--}10^{42.4}$  erg s<sup>-1</sup>). The ELGs are discussed further in §5.

<sup>8</sup> Defined as the ratio of the hard-band count rate to the soft-band count rate.

<sup>9</sup> Although we note that it is also within the range typically found for nearby X-ray faint ellipticals and S0s (e.g., Irwin & Sarazin 1998).

#### 4.1.2. Absorption-Line Galaxies

We find that three of the nine (33%) X-ray-detected ALGs have radio counterparts, while three of the four (75%) radio-detected ALGs have X-ray counterparts. In contrast to the ELGs, the ALGs have predominantly elliptical or S0 morphologies. Interestingly, only one of the X-ray-detected ALGs is clearly an AGN at X-ray energies, although another two are identified as AGN at radio wavelengths. These two are the FR I radio galaxy, CXOHDFN 123644.4+621133, and the variable radio source, CXOHDFN 123652.9+621444 (R98). As also found for the X-ray/radio ELGs, the individual X-ray constraints on these sources are poor. We can, however, gain some insight into their nature by stacking their X-ray emission. The average X-ray band ratio of the three X-ray/radio ALGs is  $0.26^{+0.09}_{-0.07}$  (corresponding to  $\Gamma = 1.90^{+0.17}_{-0.15}$ ) and is similar to that for the X-ray/radio ELGs.<sup>9</sup> By comparison, the average band ratio of the X-ray-detected ALGs that lack radio counterparts is  $0.62^{+0.14}_{-0.12}$  (corresponding to  $\Gamma = 1.28 \pm 0.19$ ), implying the possibility of different X-ray emission mechanisms at work. The X-ray luminosities of the three X-ray/radio matched ALGs are comparable to the most luminous galaxies in the ELG sample (i.e.,  $L_{0.5\text{--}8.0 \text{ keV}} \sim 10^{41.7}\text{--}10^{42.4}$  erg s<sup>-1</sup>), and they are generally more luminous than the X-ray-detected ALGs that lack radio counterparts (i.e.,  $L_{0.5\text{--}8.0 \text{ keV}} \sim 10^{39.6}\text{--}10^{41.9}$  erg s<sup>-1</sup>). Such a correspondence between X-ray and radio emission mechanisms might be expected from compact low-luminosity AGN (e.g. Ho 1999) or radio jets (e.g. Harris & Krawczynski 2002), but not from stellar processes. Unfortunately, we cannot confirm the origin of the X-ray emission in these ALGs with the current X-ray data.

#### 4.2. Optically Bright AGN

There are a total of 13 sources that lie between  $-1 \lesssim \log(f_X/f_I) \lesssim +1$  and are classified as optically bright AGN ( $I < 24$ ; OBAGN). Nearly all are confirmed AGN following the criteria listed in §3. Five of the 13 (38%) X-ray-detected OBAGN have radio counterparts, while all three (100%) radio-detected OBAGN have X-ray counterparts.

In the nearby Universe, the X-ray spectral properties of luminous AGN are found to be quite complex and often have a variety of emission and absorption features (e.g., Reynolds 1997; Turner et al. 1997; George et al. 1998; Kaspi et al. 2002). In addition to the commonly seen featureless continua, X-ray spectra of AGN can also exhibit soft X-ray excesses (e.g., Brandt, Mathur, & Elvis 1997; Brandt 1999) and absorption via either (1) “toroidal” or other material very close to the active nucleus (e.g., warm absorbers; Reynolds 1997; George et al. 1998) or (2) material associated with circumnuclear starbursts (e.g., Turner et al. 1998; Levenson, Weaver, & Heckman 2001).

The wide range of photon indices we find for our higher redshift OBAGN is qualitatively consistent with the spectral variety seen at low redshifts (see column 7 of Table 1). Interestingly, we find a distinction among the X-ray spectral slopes of the OBAGN in terms of their radio emission. The average X-ray band ratio of the radio-detected OBAGN is  $0.87 \pm 0.04$  (corresponding to  $\Gamma = 0.95 \pm 0.04$ ), while the average band ratio is  $0.39 \pm 0.02$  (corresponding to  $\Gamma = 1.64 \pm 0.04$ ) for radio-undetected OBAGN. Even after excluding the X-ray bright-

est source within the radio-detected OBAGN sample (CXOHDFN 123646.3+621404.6), the average band ratio is still  $0.56 \pm 0.04$  (corresponding to  $\Gamma = 1.36 \pm 0.07$ ). If we assume that the OBAGN have intrinsically similar underlying X-ray continuum shapes, then the above result implies that the radio-detected OBAGN are more highly obscured at soft X-ray energies than the radio-undetected OBAGN. To examine the cause of this spectral difference, we consider the radio and optical (morphological) properties of the OBAGN below.

X-ray luminous AGN in the local Universe typically have contributions to their 1.4 GHz radio emission from both star formation processes and their active nuclei. In fact, the fractions of such objects with 1.4 GHz emission dominated by global star formation and AGN appear to be roughly comparable (e.g., Wilson 1988; Colbert et al. 1996; J. Gallimore 2002 and J. Ulvelstad 2002, priv. comm.). The radio spectral indices and classifications of the OBAGN in Figure 2, coupled with the fact that their radio luminosity densities are generally modest (i.e., only two OBAGN have detections or limits above  $L_{1.4 \text{ GHz}} \sim 10^{24} \text{ W Hz}^{-1}$ ), similarly suggest that star formation activity contributes substantially to the 1.4 GHz emission in at least two of the five radio-detected OBAGN (CXOHDFN J123635.6+621424, CXOHDFN J123642.2+621545, and CXOHDFN J123655.8+621201). Interestingly, the two radio-detected OBAGN with clear starburst-type radio signatures also appear to have slightly flatter X-ray spectral slopes than those with AGN-type signatures (compare the values in Table 1).

Optically, 11 of the 13 OBAGN have been imaged by *HST*.<sup>10</sup> We find that the radio-undetected OBAGN generally have more pronounced nuclear components (e.g., three are point-like) than the radio-detected OBAGN and are therefore likely to be less obscured at optical wavelengths. This fact lends further support to the X-ray spectral dichotomy above. Even among the radio-detected OBAGN themselves, we find slight morphological differences. For instance, the two OBAGN with starburst-type radio spectral slopes have spiral and irregular morphologies with little or no apparent nuclear enhancements, while the three OBAGN with AGN-type radio spectral slopes have elliptical or bulge-dominated spiral morphologies with moderate nuclear enhancements.

Taken together, the X-ray, optical, and radio properties suggest that (1) OBAGN with starburst-like optical and radio properties make up a sizable minority of the population (perhaps  $\sim 20\%$  of the OBAGN population; see also Heckman et al. 1995 and Maiolino et al. 1997) and (2) such sources tend to be more highly obscured at optical and radio wavelengths compared to other types of OBAGN. At low redshifts, the star formation activity from such sources, sometimes called “X-ray-loud composite galaxies,” is often found to be circumnuclear in nature (perhaps as close as  $\sim 100$  pc from the central engine) and it is thought to be directly responsible for the absorption seen at X-ray energies (e.g., Levenson et al. 2001). While we lack the X-ray and radio spatial resolution needed to address this properly, our findings are at least consistent with such a scenario.

Finally, starburst-obscured AGN have been postulated to be important contributors to the cosmic X-ray background (XRB), possibly outnumbering brighter unobscured AGN by 100 to 1 (Fabian et al. 1998). Our findings clearly support the notion that such a population of AGN exists, even at optical magnitudes

of  $I < 24$ . However, the relative number of starburst-obscured OBAGN is clearly much smaller than predicted, indicating that either the majority of the presumed starburst-obscured AGN population lies at fainter optical magnitudes and presumably higher redshifts (see §4.3) or that the overall spectral “hardening” of the extragalactic X-ray background (XRB) is produced by a different mechanism altogether.

#### 4.3. The Optically Faint X-ray and Radio Sources

Due to the optical magnitudes of the optically faint ( $I \geq 24$ ) X-ray and radio sources (OFXs and OFRs), their nature remains mostly uncertain. The best available constraints on these sources to date suggest that they are comprised of luminous dust-enshrouded starburst galaxies and luminous obscured AGN at  $z \sim 1-3$ , and perhaps a few extreme redshift ( $z > 6$ ) AGN (Richards et al. 1999; Paper VI). We find that seven of the 23 (30%) OFXs have radio counterparts, while seven of the 12 (58%) OFRs have X-ray counterparts. Three of the radio-detected OFXs have X-ray spectral slope constraints that are quite hard (VLA J123651+621221, VLA J123707+621408, and VLA J123711+621325; see Table 1) and imply obscured AGN activity, while the X-ray spectral slope of a fourth radio-detected OFX (VLA 123655.8+621201) is ambiguous. If we stack the three radio-detected OFXs that lack X-ray spectral constraints (CXOHDFN J123636.9+621320.3, CXOHDFN J123642.1+621331.4, and CXOHDFN J123646.1+621448.9), we find a stacked band ratio of  $0.28^{+0.17}_{-0.14}$  ( $\Gamma = 1.85^{+0.31}_{-0.28}$ ). This ratio is significantly different from that found for both the bright radio-detected OFXs and the OFX population overall ( $0.93 \pm 0.06$ , or equivalently  $\Gamma = 0.88 \pm 0.07$ ; see also Paper VI), and it suggests that the origin of the X-ray emission in the faintest radio-detected OFXs may be due to star formation or Seyfert-luminosity, unobscured AGN. Interestingly, the radio spectral indices, classifications, and luminosity density ranges (assuming  $z \sim 1-3$ ) for five of the seven radio-detected OFXs (or 15% of all OFXs) suggest that star formation activity is likely to dominate the 1.4 GHz emission. Thus, to conclude the question of whether starburst-obscured AGN are important contributors to the XRB (see §4.2), we find that the relative number of OFXs that host both obscured AGN and luminous (i.e.  $L_{1.4 \text{ GHz}} \gtrsim 10^{23}$ ) starbursts in the CDF-N is also much smaller than predicted by Fabian et al. (1998).

## 5. DISCUSSION

Our analysis of the 1 Ms CDF-N X-ray and 1.4 GHz radio samples indicates a high degree of overlap between the two source populations and generally confirms the range of source types discovered previously in Papers II and IV. The highest matching fraction arises among the X-ray- and radio-detected ELGs and points to a potential link between the X-ray and radio emission in star-forming galaxies. The ALG population, on the other hand, appears to contain a variety of source types, including AGN and normal elliptical/S0 galaxies. Among the OBAGN population, those which are radio-detected appear to be on average more obscured than those which are radio-undetected. This enhanced obscuration may be due to active star formation occurring in these sources, as implied by their starburst-type radio properties and optical morphologies. Finally, the radio-detected OFXs appear to comprise

<sup>10</sup> The calibrated *HST* I-band flanking field images of the HDF-N were retrieved from the *HST* archive (<http://archive.stsci.edu/>) and were reduced using standard methods.



both highly-obscured AGN and unobscured AGN/star-forming galaxies. A small fraction (i.e., seven out of 36) of the OBAGN and OFXs display signs of starburst-obscured AGN from their radio properties. As such, these sources do not appear to be dominant contributors to the XRB. We cannot completely rule out the Fabian et al. (1998) model, however, since several of the remaining X-ray-detected AGN could still host weak (i.e.  $L_{1.4 \text{ GHz}} \lesssim 10^{23}$ ) starbursts.

The X-ray/radio matched ELGs are particularly important from a cosmological standpoint, as they comprise  $\approx 35\%$  of the X-ray source population below X-ray fluxes of  $5 \times 10^{-16} \text{ erg cm}^{-2} \text{ s}^{-1}$  and further mark the emergence of a population of star-forming galaxies discovered in previous X-ray studies (e.g., Paper II; Paper IV; Paper XI; Tozzi et al. 2001). We further investigate below the properties of this faint X-ray source population.

### 5.1. An X-ray/radio Correlation?

Radio emission, because of its tight linear relationship with FIR emission and its relatively short lifetime due to electron diffusion, is often used as an estimator of the recent star formation rate (SFR; e.g., Condon 1992; Yun et al. 2001). To determine whether the X-ray emission can likewise be used as an indicator of the SFR, we compare the  $K$ -corrected full-band X-ray luminosities and 1.4 GHz radio luminosity densities of the CDF-N ELGs in Figure 4.<sup>11</sup> The rest-frame X-ray luminosities of the sources are calculated as

$$L_{0.5-8.0 \text{ keV}} = 4 \pi d_L^2 f_{0.5-8.0 \text{ keV}} (1+z)^{\Gamma-2} \text{ erg s}^{-1} \quad (1)$$

and the rest-frame radio luminosity densities as

$$L_{1.4 \text{ GHz}} = 4 \pi d_L^2 S_{1.4 \text{ GHz}} 10^{-36} (1+z)^{\alpha-1} \text{ W Hz}^{-1}, \quad (2)$$

where  $d_L$  is the luminosity distance (cm),  $f_X$  is the X-ray flux ( $\text{erg cm}^{-2} \text{ s}^{-1}$ ),  $\Gamma$  corresponds to the photon index,  $S_{1.4 \text{ GHz}}$  is the 1.4 GHz flux density ( $\mu\text{Jy}$ ), and  $\alpha$  corresponds to the radio spectral index (see Tables 1 and 2). We used the actual measured  $\Gamma$  and  $\alpha$  values for the  $K$ -corrections to the CDF-N ELGs when available, or  $\Gamma = 2.0$  and  $\alpha = 0.8$  otherwise. At the redshifts of the sources ( $z \sim 0.0 - 1.3$ ), the typical  $K$ -corrections are not large.

Since the majority of the ELGs have upper limits at either X-ray or radio wavelengths, we need to use survival analysis techniques to account properly for the many upper limits when searching for a correlation; we employ the ASURV statistical package (v1.2; LaValley, Isobe, & Feigelson 1992), which implements the methods presented in Feigelson & Nelson (1985) and Isobe, Feigelson, & Nelson (1986) for censored datasets.

Among the 20 CDF-N ELGs, six have X-ray upper limits and six have radio upper limits. To establish whether a significant correlation exists between the X-ray and radio emission, we used the generalized Kendall's Tau, as it is most applicable for censored datasets with a small number of points (i.e.,  $n < 30$ ). The X-ray and radio emission in ELGs are found to be correlated at an  $\approx 2.7\sigma$  significance level. To counter the sparse sampling of the CDF-N ELGs at low luminosities, we also consider the 102 nearby late-type galaxies (i.e., non-AGN sources

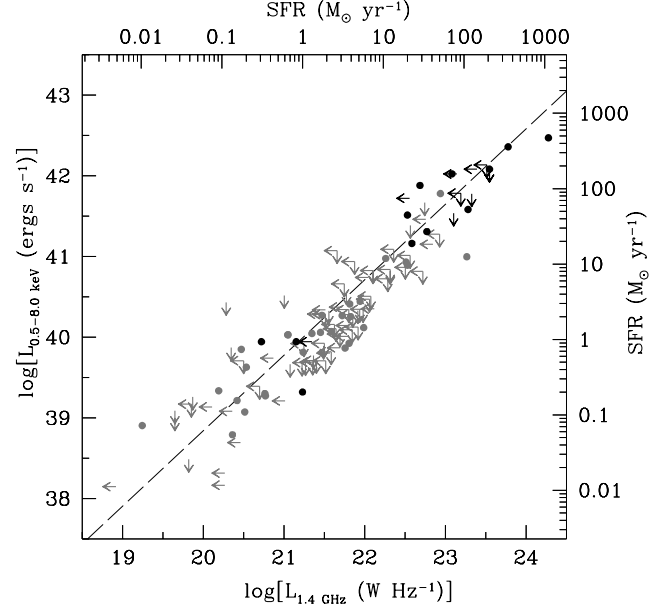


FIG. 4.— A comparison of full-band X-ray luminosity versus 1.4 GHz luminosity density for the 20 CDF-N X-ray- and radio-detected ELGs (black). Also plotted are 102 nearby galaxies (gray) from the study of Shapley et al. (2001). The luminosities have been  $K$ -corrected using the average spectral indices calculated in §4.1.1. Filled circles indicate X-ray/radio matched sources, while arrows signify  $3\sigma$  source upper limits. The dashed line shows a Theil-Sen bisector regression fit to all 122 sources. The right and top axes indicate the equivalent SFRs following Equations 4 and 5.

with  $L_X > 10^{38} \text{ erg s}^{-1}$ ) from the multi-wavelength study of Shapley et al. (2001, see their Figure 6). The luminosities of the Shapley et al. late-type galaxy sample have been converted to the bands shown in Figure 4 assuming spectral slopes of  $\Gamma = 2.0$  and  $\alpha = 0.8$ , respectively. Use of the entire 122 galaxy sample dramatically improves the likelihood of an X-ray/radio correlation to an  $\approx 7.7\sigma$  significance level.

In the presence of upper limits in both variables, the two most appropriate regression techniques are the Theil-Sen (Akritas, Murphy, & LaValley 1995) and Schmitt (Schmitt 1985) methods. We have chosen to employ the Theil-Sen bisector regression method since it does not require (subjective) binning like Schmitt's method, and we use Schmitt's method only to confirm our results.<sup>12</sup> The Theil-Sen bisector regression analysis for the 122 galaxies yields the following relationship between the X-ray luminosity and radio luminosity density:

$$\log L_{0.5-8.0 \text{ keV}} = (0.935 \pm 0.073) \log L_{1.4 \text{ GHz}} + (20.141 \pm 1.650). \quad (3)$$

Schmitt's bisector regression method yields nearly identical results (i.e., a slope of  $0.91 \pm 0.17$ ), but it has larger associated uncertainties.

The X-ray/radio correlation above is consistent with the local X-ray/radio correlations found both for the Shapley et al. sample of late-type galaxies alone and for a sample of nearby star-forming systems (i.e., sources with optical "H II nuclei" from

<sup>11</sup> Ideally, we would like to make comparisons using the hard-band X-ray luminosity in order to minimize uncertainties related to the unknown and potentially large intrinsic absorption within the X-ray-detected ELGs. However, very few ELGs have hard-band detections (22%). As a compromise, we use instead the full-band X-ray luminosity since the majority of these sources are detected in this band (78%), and the full-band flux is likely to be less uncertain than the soft-band flux.

<sup>12</sup> Instead of defining variables as "independent" and "dependent," we obtained regression coefficients (slopes, intercepts, and the uncertainties in these quantities) for both  $X|Y$  and  $Y|X$ , and we then used the bisector of these regressions following Isobe et al. (1990) and Shapley et al. (2001, Appendix B) to give a more accurate estimate of the relationship between X-ray and radio emission.

the sample of Ho, Filippenko, & Sargent 1997) using *ASCA* and *BeppoSAX* (Ranalli et al. 2002). The good agreement between the local correlations and the one determined above suggests that either (1) there is relatively little evolution in the X-ray and radio emission of ELGs between  $z = 0-1$ , or (2) the X-ray and radio emission evolve together both in magnitude and on similar timescales. We further caution that the nearly linear relationship between X-ray and radio emission found in Equation 3 may not hold for X-ray luminosities below  $\sim 10^{39}$  erg s $^{-1}$  where the data are sparse. For instance, (1) LMXBs in globular clusters would have no equivalent long-lasting radio component and therefore cause the X-ray emission to saturate while the radio emission continued to decrease, or (2) the relationship between X-ray emission and SFR may not be linearly proportional for the population of X-ray binaries emitting at sub-Eddington X-ray luminosities (e.g., Grimm, Gilfanov, & Sunyaev 2002).

The physical interpretation of this correlation is complex, as a variety of emission mechanisms could contribute to the X-ray and radio emission. In local starburst galaxies, the radio emission is produced by non-thermal processes and is thought to be driven by supernovae (although the exact mechanism by which the electrons are accelerated is still unknown; Condon 1992; Bressan et al. 2002). At X-ray energies the emission is produced by high-mass X-ray binaries (HMXBs;  $kT \sim 5-15$  keV) and extended hot gas ( $kT \sim 0.5$  keV), which are both attributed to recent star formation, and low-mass X-ray binaries (LMXBs;  $kT \sim 3-8$  keV), which trace older star formation; see, e.g., the review by Petre (1993). As the majority of the ELGs lie at  $z \sim 0.4-1.3$ , their observed X-ray fluxes should be dominated by emission from HMXBs and LMXBs (i.e., emission from point sources rather than extended hot gas). The majority of the Shapley et al. sample, however, lie below  $z \sim 0.01$ , and thus their observed X-ray fluxes may have contributions from hot gas. Globally, a link between the X-ray and radio emission seems plausible, given that both are tied to the evolution of massive stars. However, on an individual HMXB/SNR basis this link remains quite difficult to test, as these two facets of massive star formation are temporally distinct. The most significant progress on the interpretation of this correlation will be from extensive *Chandra* and *XMM-Newton* studies of our own Galaxy and nearby starburst galaxies.

One interesting application of Equation 3 is that we can now use the X-ray emission to determine SFRs for ELGs (e.g., Grimm et al. 2002). Equation 13 of Yun et al. (2001) gives the relationship between the rest-frame radio luminosity density and SFR,

$$\text{SFR}(M_{\odot} \text{ yr}^{-1}) = (5.9 \pm 1.8) \times 10^{-22} L_{1.4 \text{ GHz}} (\text{W Hz}^{-1}). \quad (4)$$

Substituting Equation 3 into the above, we obtain

$$\text{SFR}(M_{\odot} \text{ yr}^{-1}) = (1.7 \pm 0.5) \times 10^{-43} L_{0.5-8.0 \text{ keV}}^{1.07 \pm 0.08} (\text{erg s}^{-1}). \quad (5)$$

The implied SFRs found for the X-ray-detected ELGs are  $\sim 0.2-450 M_{\odot} \text{ yr}^{-1}$ . Similar rates are found using the associated IR emission from many of the X-ray/radio ELGs (e.g., Elbaz et al. 2002), highlighting the consistency across wavelength bands. Again we caution that Equation 5 may not hold for X-ray luminosities below  $\sim 10^{39}$  erg s $^{-1}$  where the data are sparse.

### 5.2. An ISOCAM dichotomy?

In Paper XI, it was found that 32 of the 40 *ISOCAM*  $15\mu\text{m}$  sources were identified with ELGs but only  $\sim 50\%$  were

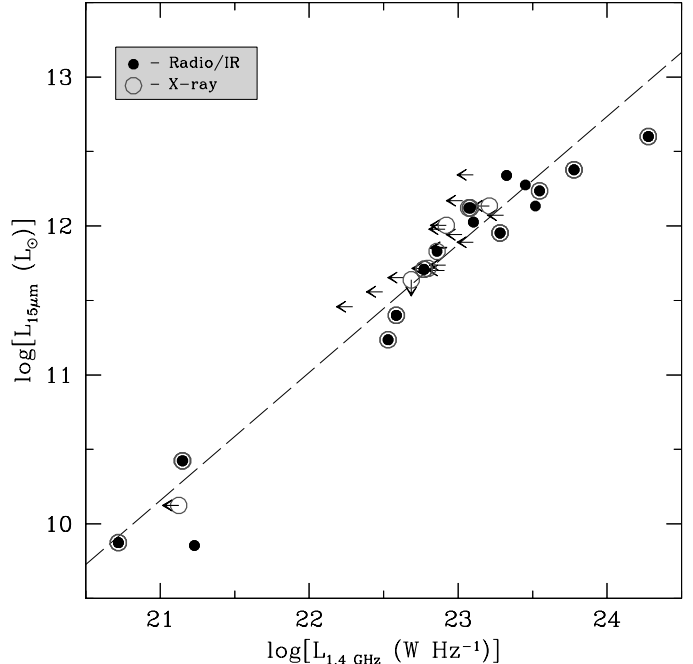


FIG. 5.— A comparison of  $15\mu\text{m}$  luminosity versus 1.4 GHz luminosity density for all *ISOCAM*  $15\mu\text{m}$  and radio-detected ELGs. Filled circles indicate  $15\mu\text{m}$ /radio matched sources, open circles denote X-ray sources, and arrows signify  $3\sigma$  source upper limits. The dashed line shows the Theil-Sen bisector regression fit to the sources.

matched with X-ray counterparts. Significantly, the X-ray-detected and X-ray-undetected  $15\mu\text{m}$  ELGs were statistically indistinguishable in terms of their  $15\mu\text{m}$  fluxes, redshifts, and optical/near-IR magnitudes, although a much larger fraction of the X-ray detected  $15\mu\text{m}$  ELGs had radio counterparts. Thus, it appears that the X-ray and radio emission from ELGs may be better matched than either one is to the  $15\mu\text{m}$  emission. This result is somewhat counter to that expected assuming, e.g., the FIR/radio correlation (e.g., Helou et al. 1985; Condon et al. 1991), and it suggests that a range of source types may exist within the faint *ISOCAM*  $15\mu\text{m}$  source population.

To test whether the  $15\mu\text{m}$  sources are a homogeneous population, we compared the  $15\mu\text{m}$ -detected and radio-detected ELGs using the complete *ISOCAM*  $15\mu\text{m}$  sample at  $> 100 \mu\text{Jy}$  of Aussel et al. (2002) and the radio sample defined in §2.2. The procedure for source matching followed that outlined in §2.3 except that  $15\mu\text{m}$  sources were matched to optical sources using a  $3''$  radius instead of  $1''$ . We find that 12 of the 13 radio-detected ELGs have  $15\mu\text{m}$  counterparts, with the one remaining radio ELG being detected by *ISOCAM* below the  $100 \mu\text{Jy}$  completeness level (see source VLA J123704.6+621429 in Table 2 and also Aussel et al. 1999). Likewise, 12 of the 32  $15\mu\text{m}$ -detected ELGs have 1.4 GHz radio counterparts, with another five ELGs detected as lower significance 1.4 GHz sources.

All of the ELGs from the  $15\mu\text{m}$ - and radio-detected samples have redshifts ( $z \sim 0.1-1.3$ ), and their resulting  $K$ -corrected  $15\mu\text{m}$  luminosities and radio luminosity densities are shown in Figure 5. The rest-frame  $15\mu\text{m}$  luminosities were  $K$ -corrected using an infrared model template of M82 (Silva et al. 1998) and the filter efficiencies of *ISOCAM* at  $15\mu\text{m}$ . Note that because we used the SED of M82 to derive the rest-frame  $15\mu\text{m}$  luminosities, the  $15\mu\text{m}$  values will likely be incorrect for sources with intrinsically different MIR colors. The radio luminosity



densities were calculated following Equation 2. For each ELG in Figure 5, we further indicate whether it was detected at X-ray energies (this includes both normal and lower significance detections).

We first note that up to 100% of the radio-detected ELGs have  $15\mu\text{m}$  counterparts, suggesting that the FIR/radio relationship extends to MIR wavelengths and moderate redshifts (a trait previously noted by Garrett et al. 2001 and Elbaz et al. 2002). A dashed line denotes the Theil-Sen bisector regression fit to the  $15\mu\text{m}$ /radio matched ELGs.

As found in Paper XI, the majority of the  $15\mu\text{m}$ -detected ELGs with radio counterparts also have X-ray counterparts, while most of the  $15\mu\text{m}$ -detected ELGs without radio counterparts do not. Moreover, most of the  $15\mu\text{m}$ -detected ELGs with radio upper limits lie to the  $15\mu\text{m}$  bright side of the regression. These two facts suggest an intrinsic bimodality in the  $15\mu\text{m}$ -detected ELGs.

We can quantify this bimodality statistically by comparing the  $15\mu\text{m}$ -to-radio luminosity ratio (i.e. reducing the dimensionality of the problem to single quantity), and then testing for whether the X-ray-detected distribution differs from the X-ray-undetected one using the Kaplan-Meier (KM) test within ASURV to account for the numerous radio upper limits. The result of the KM test indicates that the distributions have a  $P = 0.01$  probability of coming from the same parent distribution. And since the majority of the X-ray-undetected  $15\mu\text{m}$  ELGs have radio luminosity density upper limits, this difference could be even stronger.

The most likely explanation for such a dichotomy is that the  $15\mu\text{m}$ -detected ELGs with X-ray counterparts have significantly different MIR spectral energy distributions from those without them. To still be consistent with the FIR/radio correlation, these X-ray-undetected ELGs would have to have substantially warmer MIR/FIR colors than M82 (i.e., the spectral template used to  $K$ -correct our  $15\mu\text{m}$  luminosities). An enhancement to the MIR flux could be explained by either a hotter dust component or stronger emission-line features (e.g., PAH features; Puget & Leger 1989) as compared to M82. Because a hotter dust component requires more high energy photons (i.e., more X-ray emission), however, we might expect enhanced X-ray emission rather than a lack of it. Thus, the most likely explanation for the  $15\mu\text{m}$ -detected ELGs without X-ray counterparts is that they have significantly stronger emission-line features than those with X-ray counterparts.

## 6. CONCLUSIONS

Our main results are the following:

- We find a large overlap between faint X-ray and radio sources detected within  $3'$  of the HDF-N using the 1 Ms CDF-N and  $40\mu\text{Jy}$  VLA 1.4 GHz radio surveys. The matched sources exhibit a broad range of emission mechanisms, in agreement with the findings of Papers II and IV.
- The highest matching fraction is found among X-ray- and radio-detected ELGs, which are comprised of apparently normal and starburst galaxies at redshifts of  $z \sim 0.1\text{--}1.3$  thought to be undergoing recent star formation. The ELGs are distinct in terms of their X-ray, optical, and radio properties, and nearly all of them have MIR *ISOCAM* detections.

- The radio-detected ELGs make up  $\approx 35\%$  of the X-ray source population at X-ray fluxes below  $5 \times 10^{-16} \text{ erg cm}^{-2} \text{ s}^{-1}$  and further signal the emergence of a population of star-forming galaxies discovered in previous X-ray studies. The high matching fraction among the ELGs suggests that the deep  $40\mu\text{Jy}$  VLA survey at 1.4 GHz is extremely well-matched to the 1 Ms *Chandra* observation for the detection of galaxies.
- The X-ray-emitting AGN population (i.e., OBAGN + OFXs) have significantly fewer radio matches than the ELGs. These sources exhibit a range of X-ray spectral slopes suggesting many are moderately obscured. Moreover, the radio properties and optical morphologies of the harder X-ray AGN indicate that their obscuration at X-ray energies may be related to active star formation (perhaps circumnuclear). The relative numbers of such starburst-obscuring AGN, however, suggest that they are not likely to be dominant contributors to the XRB.
- A good correlation exists between X-ray luminosity and radio luminosity density for the CDF-N ELGs and nearby late-type galaxies, and it suggests that the emission mechanisms from the evolution of massive stars (e.g., the creation of HMXBs) and their eventual destruction (e.g., supernova-accelerated electrons) are intimately linked, even at moderate redshifts. This link suggests that X-ray emission can likewise be used as an indicator of the SFR. The implied SFRs found for the X-ray-detected ELGs in the CDF-N are  $\sim 0.2\text{--}450 M_{\odot} \text{ yr}^{-1}$ .
- Finally, there appear to be two statistically distinct classes of infrared star-forming galaxies detected with *ISOCAM*, one of which shows correlated X-ray and radio emission, and one which does not. This latter group is likely to have significant stronger emission-line features than the those with X-ray and radio counterparts. Confirmation of this result must await the Guaranteed Time and Great Observatories Origins Deep Survey<sup>13</sup> observations of the CDF-N with SIRTf, which will offer both deep spectroscopy and multi-band photometry at MIR wavelengths over a much larger area. We note that the X-ray exposure of the CDF-N has recently increased to 2 Ms. Thus, the robust X-ray/radio matching fraction we find with the 1 Ms CDF-N dataset also signals the need for deeper radio observations with the VLA to build upon this work.

This work would not have been possible without the support of the entire *Chandra* and ACIS teams; we particularly thank P. Broos and L. Townsley for data analysis software and CTI correction support. We thank E. Feigelson, J. Gallimore, J. H. Schmitt, and J. Ulvestad for helpful discussions, M. LaValley for providing pre-written code for the Theil-Sen estimator algorithm, A. Barger, L. Cowie, and E. Richards for kindly providing or making public their optical and radio images of the HDF-N region. and the anonymous referee for useful comments that improved the content and presentation of the paper. We gratefully acknowledge the financial support of NSF CAREER award AST-9983783 (FEB, DMA, WNB, CV), NASA

<sup>13</sup> See <http://www.stsci.edu/science/goods/>.

GSRP grant NGT5-50247 and the Pennsylvania Space Grant Consortium (AEH), NASA grant NAS 8-38252 (GPG, PI), and

NSF grant AST-9900703 (DPS).

# REFERENCES

- Akiyama, M. et al. 2000, *ApJ*, 532, 700
- Akritis, M. G., Murphy, S. A., & LaValley, M. P. 1995, *J. Amer. Stat. Assoc.*, 90, 170
- Alexander, D. M., Brandt, W. N., Hornschemeier, A. E., Garmire, G. P., Schneider, D. P., Bauer, F. E., & Griffiths, R. E. 2001, *AJ*, 122, 2156 (Paper VI)
- Alexander, D. M. et al. 2002, *ApJ*, 568, L85 (Paper XI)
- Aussel, H., Cesarsky, C. J., Elbaz, D., & Starck, J. L. 1999, *A&A*, 342, 313
- Aussel, H., et al. 2002, in preparation
- Bade, N. et al. 1998, *A&AS*, 127, 145
- Barger, A. J., Cowie, L. L., Trentham, N., Fulton, E., Hu, E. M., Songaila, A., & Hall, D. 1999, *AJ*, 117, 102
- Barger, A. J., Cowie, L. L., Brandt, W. N., Capan, P., Garmire, G. P., Hedrick, E. M., Hornschemeier, A. E., & Steffen, A. 2002, *AJ*, in press (astro-ph/0206370)
- Bauer, F. E. 2001, Ph.D. thesis, University of Virginia
- Bauer, F. E. et al. 2002, *AJ*, 123, 1163 (Paper IX)
- Bauer, F. E., Condon, J. J., Thuan, T. X., & Broderick, J. J. 2000, *ApJS*, 129, 547
- Brandt, W. N. 1999, in *High Energy Processes in Accreting Black Holes*, ed. J. Poutanen & R. Svenson (San Francisco: ASP Press), 166
- Brandt, W. N. et al. 2001a, *AJ*, 122, 1 (Paper IV)
- Brandt, W. N. et al. 2001b, *AJ*, 122, 2810 (Paper V)
- Brandt, W. N., Mathur, S., & Elvis, M. 1997, *MNRAS*, 285, L25
- Bressan, A., Silva, L., & Granato, G. L. 2002, *A&A*, in press (astro-ph/0206029)
- Brinkmann, W., Laurent-Muehleisen, S. A., Voges, W., Siebert, J., Becker, R. H., Brotherton, M. S., White, R. L., & Gregg, M. D. 2000, *A&A*, 356, 445
- Cohen, J. G., Hogg, D. W., Blandford, R., Cowie, L. L., Hu, E., Songaila, A., Shopbell, P., & Richberg, K. 2000, *ApJ*, 538, 29
- Colbert, E. J. M., Baum, S. A., Gallimore, J. F., O'Dea, C. P., & Christensen, J. A. 1996, *ApJ*, 467, 551.
- Condon, J. J. 1992, *ARA&A*, 30, 575
- Condon, J. J., Anderson, M. L., & Helou, G. 1991, *ApJ*, 376, 95
- David, L. P., Jones, C., & Forman, W. 1992, *ApJ*, 388, 82.
- Dawson, S., Stern, D., Bunker, A. J., Spinrad, H., & Dey, A. 2001, *AJ*, 122, 598
- Elbaz, D., Cesarsky, C., Chanial, P., Aussel, H., Franceschini, A., Fadda, D., & Chary, R. 2002, *A&A*, 384, 848
- Elvis, M. et al. 1994, *ApJS*, 95, 1
- Fabbiano, G. 1989, *ARA&A*, 27, 87
- Fabbiano, G., Gioia, I. M., & Trinchieri, G. 1988, *ApJ*, 324, 749.
- Fabian, A. C., Barcons, X., Almaini, O., & Iwasawa, K. 1998, *MNRAS*, 297, L11
- Feigelson, E. D., & Nelson, P. I. 1985, *ApJ*, 293, 192
- Ferguson, H. C., Dickinson, M., & Williams, R. 2000, *ARA&A*, 38, 667
- Freeman, P. E., Kashyap, V., Rosner, R., & Lamb, D. Q. 2002, *ApJS*, 138, 185.
- Garrett, M. A. 2002, *A&A*, 384, L19
- Garrett, M. A., et al. 2001, *A&A*, 366, L5
- Garrett, M. A., de Bruyn, A. G., Giroletti, M., Baan, W. A., & Schilizzi, R. T. 2000, *A&A*, 361, L41 (see also <http://www.jive.nl/~mag/hdf>)
- Gehrels, N. 1986, *ApJ*, 303, 336
- George, I. M., Turner, T. J., Netzer, H., Nandra, K., Mushotzky, R. F., & Yaqoob, T. 1998, *ApJS*, 114, 73
- Grimm, H. J., Gilfanov, R., & Sunyaev, R. 2002, *MNRAS*, submitted (astro-ph/0205371)
- Harris, D. E. & Krawczynski, H. 2002, *ApJ*, 565, 244
- Heckman, T. et al. 1995, *ApJ*, 452, 549
- Helou, G., Soifer, B. T., & Rowan-Robinson, M. 1985, *ApJ*, 298, L7
- Ho, L. C. 1999, *ApJ*, 516, 672
- Ho, L. C., Filippenko, A. V., & Sargent, W. L. W. 1997, *ApJS*, 112, 315.
- Hornschemeier, A. E. et al. 2001, *ApJ*, 554, 742 (Paper II)
- Irwin, J. A., & Sarazin, C. L. 1998, *ApJ*, 494, L33
- Isobe, T., Feigelson, E. D., Akritis, M. G., & Babu, G. J. 1990, *ApJ*, 364, 104
- Isobe, T., Feigelson, E. D., & Nelson, P. I. 1986, *ApJ*, 306, 490
- Kaspi, S. et al. 2002, *ApJS*, in press (astro-ph/0203263)
- Kellermann, K. I., Sramek, R., Schmidt, M., Shaffer, D. B., & Green, R. 1989, *AJ*, 98, 1195
- Kellermann, K. I., & Owen, F. N. 1988, in *Galactic and Extragalactic Radio Astronomy*, eds. G. L. Verschuur & K. I. Kellermann (New York: Springer)
- LaValley, M., Isobe, T., & Feigelson, E. 1992, *ASP Conf. Ser. 25: Astronomical Data Analysis Software and Systems I*, 1, 245
- Lehmann, I. et al. 2001, *A&A*, 371, 833
- Levenson, N. A., Weaver, K. A., & Heckman, T. M. 2001, *ApJ*, 550, 230
- Levenson, N. A., Cid Fernandes, R., Weaver, K. A., Heckman, T. M., & Storchi-Bergmann, T. 2001, *ASP Conf. Ser. 249: The Central Kiloparsec of Starbursts and AGN: The La Palma Connection*, 418
- Maccacaro, T., Gioia, I. M., Wolter, A., Zamorani, G., & Stocke, J. T. 1988, *ApJ*, 326, 680.
- Maiolino, R., Ruiz, M., Rieke, G. H., & Papadopoulos, P. 1997, *ApJ*, 485, 552
- Muxlow, T. W. B., Wilkinson, P. N., Richards, A. M. S., Kellermann, K. I., Richards, E. A., & Garrett, M. A. 1999, *New Astronomy Review*, 43, 623
- Petre R., 1993, in "The Nearest Active Galaxies," eds. J. Beckman, L. Colina, & H. Netzer, CSIC Press, Madrid, p. 117
- Price, R., & Duric, N. 1992, *ApJ*, 401, 81
- Puget, J. L. & Leger, A. 1989, *ARA&A*, 27, 161
- Ranalli, P., Comastri, A., & Setti, G. 2002, in "New Visions of the X-ray Universe in the XMM-Newton and Chandra Era," eds. F. Jansen (astro-ph/0202241)
- Reynolds, C. S. 1997, *MNRAS*, 286, 513
- Richards, E. A. 1999, Ph.D. Thesis, University of Virginia (R99)
- Richards, E. A. 2000, *ApJ*, 533, 611 (R00)
- Richards, E. A., Fomalont, E. B., Kellermann, K. I., Windhorst, R. A., Partridge, R. B., Cowie, L. L., & Barger, A. J. 1999, *ApJ*, 526, L73
- Richards, E. A., Kellermann, K. I., Fomalont, E. B., Windhorst, R. A., & Partridge, R. B. 1998, *AJ*, 116, 1039 (R98)
- Schmidt, M. et al. 1998, *A&A*, 329, 495
- Schmitt, J. H. M. M. 1985, *ApJ*, 293, 178
- Shapley, A., Fabbiano, G., & Eskridge, P. B. 2001, *ApJS*, 137, 139
- Silva, L., Granato, G. L., Bressan, A., & Danese, L. 1998, *ApJ*, 509, 103
- Stark, A. A., Gammie, C. F., Wilson, R. W., Bally, J., Linke, R. A., Heiles, C., & Hurwitz, M. 1992, *ApJS*, 79, 77
- Stocke, J. T. et al. 1991, *ApJS*, 76, 813.
- Turner, T. J., George, I. M., Nandra, K., & Mushotzky, R. F. 1997, *ApJ*, 488, 164.
- Turner, T. J., George, I. M., Nandra, K., & Mushotzky, R. F. 1998, *ApJ*, 493, 91.
- Tozzi, P. et al. 2001, *ApJ*, 562, 42
- Williams, R. E. et al. 1996, *AJ*, 112, 1335
- Wilson, A. S. 1988, *A&A*, 206, 41
- Windhorst, R. A., Miley, G. K., Owen, F. N., Kron, R. G., & Koo, D. C. 1985, *ApJ*, 289, 494
- Yun, M. S., Reddy, N. A., & Condon, J. J. 2001, *ApJ*, 554, 803

TABLE 1  
 3' X-RAY SAMPLE

(1) CXOHDFN Source	(2) $I$	(3) $S_{1.4 \text{ GHz}}$	(4) $S_{8.5 \text{ GHz}}$	(5) $\alpha_r$	(6) $f_{0.5-8.0 \text{ keV}}$	(7) $\Gamma$	(8) $S_{15 \mu\text{m}}$	(9) $z$	(10) $L_{0.5-8.0 \text{ keV}}$	(11) Sp. Type	(12) Category
123627.3+621257	21.94	—	<15.3 <sup>a</sup>	...	<1.4 <sup>c</sup>	...	—	1.221	42.23	EI	ELG
123627.3+621308	26.14	—	<15.3 <sup>a</sup>	...	1.1	...	—	...	...	—	OF
123627.5+621218	>27.10	—	<16.1 <sup>a</sup>	...	3.1	1.48	—	...	...	—	OF
123627.8+621158	23.38	—	<17.0 <sup>a</sup>	...	21.6	-0.17	—	...	...	—	AGN
123633.5+621418	25.18	<17.0 <sup>a</sup>	<12.0	...	10.0	1.74	—	3.408	44.21	Q	OF (AGN)
123633.7+621313	25.79	<24.9 <sup>a</sup>	<8.7	...	10.6	<-0.29	—	...	...	—	OF (AGN)
123633.9+621327	23.89	<25.0 <sup>a</sup>	<8.8	...	<1.1 <sup>c</sup>	...	—	...	...	—	ALG <sup>d</sup>
123634.4+621213	19.21	233.0	56.5	0.74	4.3	>1.86	448	0.458	41.88	I	ELG
123634.5+621240	22.34	230.0	52.6	0.74	3.1	...	363	1.219	42.46	E	ELG <sup>d</sup>
123635.3+621110	20.45	<25.6 <sup>a</sup>	<13.6 <sup>a</sup>	...	9.5	0.99	<100	0.410	41.94	A	ALG (AGN)
123635.3+621152	24.30	<25.0 <sup>a</sup>	<9.5 <sup>a</sup>	...	2.9	...	—	...	...	—	OF
123635.6+621424	23.01	87.8	13.2	1.05 <sup>b</sup>	29.7	0.30	441	2.005	43.23	E	AGN
123636.6+621346	20.94	<24.8 <sup>a</sup>	<7.8 <sup>a</sup>	...	101.0	1.82	353	0.960	43.99	Q	AGN
123636.7+621156	21.42	<24.9 <sup>a</sup>	<8.4 <sup>a</sup>	...	49.4	1.74	<78	0.557	43.11	I	AGN
123636.9+621320	>26.49	50.0	7.2 <sup>a</sup>	1.07 <sup>b</sup>	2.0	...	—	...	...	—	OF
123637.0+621134	18.60	99.0 <sup>W</sup>	17.5	0.96 <sup>b</sup>	<1.2 <sup>c</sup>	...	300	0.078	39.80	I	ELG
123638.5+621339	22.31	<24.6 <sup>a</sup>	<6.8 <sup>a</sup>	...	5.8	<-0.08	52	0.357	41.18	I	AGN
123639.0+621041	>27.10	—	<15.3 <sup>a</sup>	...	5.6	1.44	—	...	...	—	OF
123639.6+621230	23.83	<24.4 <sup>a</sup>	<6.2 <sup>a</sup>	...	6.9	1.87	<41	3.479	44.16	EQ	AGN
123639.9+621250	21.00	36.4 <sup>a</sup>	9.8	0.55 <sup>b</sup>	2.7	...	295	0.848	42.17	I	ELG
123640.8+621041	24.69	—	<14.2 <sup>a</sup>	...	21.9	0.69	—	...	...	—	OF (AGN)
123641.8+621132	19.76	23.2 <sup>a</sup>	<8.4 <sup>a</sup>	>0.56 <sup>b</sup>	3.8	...	236	0.089	40.22	EI	ELG
123642.1+621331	24.98	467.0	79.9	0.94	2.5	...	23	4.424	43.28	E	OF (AGN)
123642.2+621545	21.21	150.0	53.6	0.50	32.0	1.29	459	0.857	43.21	I	AGN
123644.4+621133	21.26	1290.0	599.0	0.30	2.1	...	<47	1.010	42.26	A	ALG (AGN)
123646.1+621448	25.21	124.0	13.3	0.84	1.4	...	—	...	...	—	OF
123646.3+621404	21.07	179.0	190.0	-0.04	228.0	0.58	107	0.962	43.88	Q	AGN
123646.4+621529	21.80	—	<14.8 <sup>a</sup>	...	5.3	1.32	<92	...	...	—	ALG <sup>d</sup>
123648.0+621019	25.71	—	<16.1 <sup>a</sup>	...	9.6	0.10	104	...	...	—	OF (AGN)
123648.1+621308	20.29	<24.0 <sup>a</sup>	<5.5 <sup>a</sup>	...	7.5	1.17	<22	0.476	42.01	I	ELG
123648.3+621426	18.60	25.1 <sup>a</sup>	9.8	0.57 <sup>b</sup>	1.5	...	307	0.139	40.21	E	ELG
123648.3+621456	26.27	<25.0 <sup>a</sup>	<9.4 <sup>a</sup>	...	11.2	0.61	<52	...	...	—	OF (AGN)
123649.4+621346	18.00	<24.2 <sup>a</sup>	<5.6 <sup>a</sup>	...	0.9	...	—	0.089	39.58	A	ALG
123649.7+621313	21.38	49.2	22.0	0.72	1.5	...	115	0.475	41.36	I	ELG
123651.1+621031	20.17	95.0	26.0	0.74	3.0	...	341	0.410	41.52	I	ELG
123651.3+621051	23.55	—	<10.5 <sup>a</sup>	...	12.7	<-0.11	—	...	...	—	AGN
123651.8+621221	25.80	49.3	16.8	0.71	28.1	0.37	48	2.750	43.35	—	OF (AGN)
123651.8+621505	24.65	—	<10.7 <sup>a</sup>	...	21.3	1.43	—	...	...	—	OF
123652.9+621444	18.92	168.0	185.0	-0.12	5.7	1.92	<53	0.322	41.67	A	ALG (AGN)
123653.4+621139	22.05	65.7	15.1	0.77	2.2	...	180	1.275	42.45	EA	ELG
123653.6+621115	22.47	<24.9 <sup>a</sup>	<8.3 <sup>a</sup>	...	<1.4 <sup>c</sup>	...	<80	...	...	—	ELG?
123654.6+621111	26.07	<25.0 <sup>a</sup>	<8.8 <sup>a</sup>	...	7.7	0.28	—	...	...	—	OF (AGN)
123655.4+621311	21.92	<23.6 <sup>a</sup>	12.3	<0.36	12.7	1.50	23	0.968	43.00	A	AGN
123655.8+621201	24.13	24.3 <sup>a</sup>	<6.7 <sup>a</sup>	>0.71 <sup>b</sup>	4.3	1.36	—	1.140 <sup>P</sup>	42.54	—	OF (AGN?)
123656.6+621245	20.24	<24.2 <sup>a</sup>	<5.6 <sup>a</sup>	...	1.1	...	<28	0.518	41.32	A	ALG
123656.6+621513	26.20	—	<13.2 <sup>a</sup>	...	6.0	<-0.17	—	...	...	—	OF (AGN)
123656.9+621301	22.66	49.5	7.6	1.04 <sup>b</sup>	8.6	1.77	<45	0.474	42.20	E	ELG <sup>d</sup>
123657.3+621024	22.35	—	<17.1 <sup>a</sup>	...	2.7	...	—	0.847	41.86	E	ELG
123657.5+621210	20.71	<24.4 <sup>a</sup>	<6.2 <sup>a</sup>	...	2.4	...	<80	0.665	41.89	A	ALG
123658.8+621022	24.28	—	<18.5 <sup>a</sup>	...	12.0	<-0.34	—	...	...	—	OF (AGN)
123658.8+621435	20.40	<24.4	11.4	<0.42	73.1	1.48	<50	0.678	43.41	I	AGN
123700.4+621509	23.89	—	<14.7 <sup>a</sup>	...	16.6	1.11	—	...	...	—	AGN
123702.0+621123	18.53	<25.3 <sup>a</sup>	<10.9 <sup>a</sup>	...	1.5	...	162	0.136	40.21	I	ELG
123702.6+621244	23.97	<24.7 <sup>a</sup>	<7.2 <sup>a</sup>	...	3.5	...	—	...	...	—	AGN
123704.1+621155	25.66	<25.1 <sup>a</sup>	<9.7 <sup>a</sup>	...	1.6	...	—	...	...	—	OF
123704.6+621429	20.78	25.7 <sup>a</sup>	<12.5 <sup>a</sup>	>0.37 <sup>b</sup>	2.3	...	72	0.561	41.70	I	ELG
123707.2+621408	24.64	45.3	29.0	0.29	10.0	0.50	—	...	...	—	OF (AGN)
123711.4+621331	22.96	132.0	31.1	0.69	2.9	...	—	1.110 <sup>P</sup>	42.37	—	ALG <sup>d</sup>
123712.0+621325	24.87	53.9	13.5 <sup>a</sup>	0.76 <sup>b</sup>	5.6	<0.09	—	...	...	—	OF (AGN)
123712.1+621211	25.90	—	<17.7 <sup>a</sup>	...	1.9	...	—	...	...	—	OF
123712.7+621342	>26.20	—	<18.6 <sup>a</sup>	...	1.6	...	—	...	...	—	OF
123714.4+621221	23.05	—	<21.3 <sup>a</sup>	...	1.7	...	—	1.084	42.19	E	ELG <sup>d</sup>

Note. — Col. 1: Source name given as CXOHDFN JHHMSS.S+DDMMSS. Col. 2:  $I$ -band magnitude. See §2.3 for details. Cols. 3 & 4: 1.4 GHz and 8.5 GHz catalog radio flux densities in  $\mu\text{Jy}$ , respectively. An “a” indicates that the 1.4 GHz or 8.5 GHz flux densities have been measured using the publicly available images down to  $3\sigma$  limit. A “—” indicates that the source lies outside of the publicly available VLA 1.4 GHz image and thus the source has no detection down to a  $5\sigma$  flux density limit of  $\sim 40 \mu\text{Jy}$  at 1.4 GHz. The 1.4 GHz flux density for the source denoted by a “W” is taken from the the WSRT 1.4 GHz catalog of Garrett et al. (2000). Col. 5: Radio spectral slope,  $\alpha_r$ , calculated using 1.4 GHz and 8.5 GHz fluxes measured in their respective  $3'' \times 5$  convolved images (R00). A “b” indicates that the spectral slopes have been calculated using lower significance 1.4 GHz and/or 8.5 GHz flux densities measured from the publicly available  $1'' \times 9$  and  $3'' \times 5$  convolved images, respectively. As such, these spectral slopes should therefore only be considered approximate since the beamsizes of the 1.4 GHz and 8.5 GHz images have not been properly matched. Col. 6: Observed 0.5–8.0 keV flux calculated assuming the value of  $\Gamma$  listed in Col. 7 or  $\Gamma = 1.4$  if not listed (see Paper V for details), in units of  $10^{-16} \text{ erg cm}^{-2} \text{ s}^{-1}$ . Sources denoted by a “c” are detected only in the 0.5–2.0 keV band. We calculated X-ray upper limits following §3.2.1 of Paper V. Col. 7: X-ray power-law photon index,  $\Gamma$ , computed from the band ratio (i.e., the ratio of 2.0–8.0 keV count rate, or  $3\sigma$  upper limit, to 0.5–2.0 keV count rate; see Paper V for details). Note that many sources lack  $\Gamma$  values due to their low number of counts. Col. 8: *ISOCAM*  $15 \mu\text{m}$  flux density as reported in Aussel et al. (1999, 2002). Three  $\sigma$   $15 \mu\text{m}$  upper limits were computed for all X-ray sources within the complete *ISOCAM* area following Aussel et al. (2002). A “—” indicates that the source lies outside of the *ISOCAM* field of view. Col. 9: Spectroscopic redshift from the catalogs of Cohen et al. (2000) or Dawson et al. (2001). The two redshifts denoted by “P’s” are photometric and were obtained from the catalog presented in Paper IX. Col. 10: Logarithm of the absorption-corrected rest-frame 0.5–8.0 keV luminosities, calculated assuming the unabsorbed spectrum is a  $\Gamma = 2.0$  power law, in units of  $\text{erg s}^{-1}$ . Col. 11: Spectral classification from the catalogs of Cohen et al. (2000), or if from Dawson et al. (2001) or Barger et al. (2002), converted to the Cohen et al. (2000) classification scheme. Col. 12: Source classification category (see §3). An “d” indicates that the source lies in the AGN region of Figure 3 but is considered to be part of the galaxy sample. Entries appended with a “?” are tentative.

TABLE 2  
3' 1.4 GHz SAMPLE

(1) VLA Source	(2) $I$	(3) $S_{1.4 \text{ GHz}}$	(4) $S_{8.5 \text{ GHz}}$	(5) $\alpha_r$	(6) $f_{0.5-8.0 \text{ keV}}$	(7) $\Gamma$	(8) $S_{15 \mu\text{m}}$	(9) $z$	(10) $L_{0.5-8.0 \text{ keV}}$	(11) Sp. Type	(12) Radio Type	(13) Category
123634.4+621212	19.21	233.0	56.5	0.74	4.3	>1.86	448	0.458	41.88	I	S	ELG
123634.5+621241	22.34	230.0	52.6	0.74	3.1	...	363	1.219	42.47	E	S	ELG <sup>d</sup>
123635.6+621424	23.01	87.8	13.2 <sup>a</sup>	1.05 <sup>b</sup>	29.7	0.30	441	2.005	43.23	E	S	AGN
123636.9+621320	>26.50	50.0	7.2 <sup>a</sup>	1.07 <sup>b</sup>	2.0	...	—	...	...	—	U	OF
123640.7+621010	25.84	86.8	29.2	0.44	<1.5	...	—	...	...	—	U	OF
123642.0+621331	24.98	467.0	79.9	0.94	2.5	...	23	4.424	43.28	E	U	OF (AGN)
123642.2+621545	21.21	150.0	53.6	0.50	32.0	1.29	459	0.857	43.21	I	S	AGN
123644.3+621133	21.26	1290.0	599.0	0.30	2.1	...	<41	1.010	42.26	A	A	ALG (AGN)
123646.0+621448	25.21	124.0	13.3	0.84	1.4	...	—	...	...	—	U	OF
123646.3+621404	21.07	179.0	190.0	-0.04	228.0	0.58	107	0.962	43.88	Q	A	AGN
123646.6+621226	>26.20	72.0	15.6 <sup>a</sup>	0.85 <sup>b</sup>	<0.7	...	<100	...	...	—	U	OF
123646.7+621445	23.22	117.0	<9.1 <sup>a</sup>	>1.42 <sup>b</sup>	<1.0	...	—	...	...	—	S	ALG
123649.7+621312	21.38	49.2	22.0	0.72	1.5	...	115	0.475	41.36	I	S	ELG
123651.1+621030	20.17	95.0	26.0	0.74	3.0	...	341	0.410	41.52	I	S	ELG
123651.7+621221	25.80	49.3	16.8	0.71	28.1	0.37	48	2.750	43.35	—	S	OF (AGN)
123652.9+621444	18.92	168.0	185.0	-0.12	5.7	1.92	<53	0.322	41.67	A	A	ALG (AGN)
123653.4+621139	21.96	65.7	15.1	0.77	2.2	...	180	1.275	42.45	EA	S	ELG
123654.7+621039	>26.20	48.2	<13.7 <sup>a</sup>	>1.00	<0.6	...	—	...	...	—	U	OF
123656.6+621207	>26.20	46.2	<6.7 <sup>a</sup>	>1.07	<0.9	...	—	...	...	—	U	OF
123656.9+621302	22.66	49.5	7.6 <sup>a</sup>	1.04 <sup>b</sup>	8.6	1.77	—	0.474	42.20	E	S	ELG <sup>d</sup>
123659.9+621449	21.20	47.0	<12.1 <sup>a</sup>	>0.75 <sup>b</sup>	<1.1	...	295	0.762	<41.46	EI	U	ELG
123701.5+621146	25.30	128.0	29.5	0.67	1.4	...	<100	0.884	41.70	E	S	OF
123702.8+621401	22.17	41.4	<9.5 <sup>a</sup>	>0.79	<1.2 <sup>c</sup>	...	144	1.243	<41.98	E	S	ELG
123705.8+621153	20.60	52.5	<11.9 <sup>a</sup>	>0.82 <sup>b</sup>	<1.3	...	431	0.904	<41.69	I	S	ELG
123707.2+621408	24.64	45.3	29.0	0.29	10.0	0.50	—	...	...	—	U	OF (AGN)
123707.9+621121	25.30	60.3	6.2 <sup>a</sup>	1.26 <sup>b</sup>	<1.4	...	—	...	...	—	U	OF
123711.3+621331	22.96	132.0	31.1	0.69	2.9	...	—	1.110 <sup>P</sup>	42.37	—	S	ALG?
123711.9+621325	24.87	53.9	13.5 <sup>a</sup>	0.76 <sup>b</sup>	5.6	<0.09	—	...	...	—	S	OF (AGN)

Note. — Col. 1: Source name given as VLA JHHMMSS.S+DDMMSS. Col. 2:  $I$ -band magnitude. See §2.3 for details. Cols. 3 & 4: 1.4 GHz and 8.5 GHz catalog radio flux densities in  $\mu\text{Jy}$ , respectively. An “a” indicates that the 8.5 GHz flux densities have been measured using the publicly available image down to a  $3\sigma$  limit. Col. 5: Radio spectral slope,  $\alpha_r$ , calculated using the 1.4 GHz and 8.5 GHz fluxes measured in their respective 3''/5 convolved images (R00). A “b” indicates that the spectral slopes have been calculated using lower significance 8.5 GHz flux densities measured from the publicly available 3''/5 convolved image. As such, these spectral slopes should therefore only be considered approximate since the beamsizes of the 1.4 GHz and 8.5 GHz images have not been properly matched. Col. 6: Observed 0.5–8.0 keV flux calculated assuming the value of  $\Gamma$  listed in Col. 7 or  $\Gamma = 1.4$  if not listed (see Paper V for details), in units of  $10^{-16} \text{ erg cm}^{-2} \text{ s}^{-1}$ . Sources denoted by a “c” are detected only in the 0.5–2.0 keV band. We calculated X-ray upper limits following §3.2.1 of Paper V. Col. 7: X-ray power-law photon index,  $\Gamma$ , computed from the band ratio (i.e., the ratio of 2.0–8.0 keV count rate, or  $3\sigma$  upper limit, to 0.5–2.0 keV count rate; see Paper V for details). Note that many sources lack  $\Gamma$  values due to their low number of counts. Col. 8: *ISOCAM*  $15\mu\text{m}$  flux density as reported in Aussel et al. (1999, 2002). Three  $\sigma$   $15\mu\text{m}$  upper limits were computed for all X-ray sources within the complete *ISOCAM* area following Aussel et al. (2002). A “—” indicates that the source lies outside of the *ISOCAM* field of view. Col. 9: Redshift from the catalogs of Cohen et al. (2000) or Dawson et al. (2001). The one redshift denoted by a “P” is photometric and was obtained from the catalog presented in Paper IX. Col. 10: Logarithm of the absorption-corrected rest-frame 0.5–8.0 keV luminosities, calculated assuming the unabsorbed spectrum is a  $\Gamma = 2.0$  power law, in units of  $\text{erg s}^{-1}$ . Col. 11: Spectral classification from the catalogs of Cohen et al. (2000), or if from Dawson et al. (2001) or Barger et al. (2002), converted to the Cohen et al. (2000) classification scheme. Col. 12: Radio classification from R99. Col. 13: Source classification category (see §3). An “d” indicates that the source lies in the AGN region of Figure 3 but is considered to be part of the galaxy sample. Entries appended with a “?” are tentative.